scientific reports

OPEN

Cell spheroid micromechanics under large deformations

Dimosthenis Giannopoulos[1], Maja Schlittler[2], Marzia De Bortoli[2], Raffaele Coppini[3], Mina Petrovic[4], Elisabetta Cerbai[3], Gerhard J. Schütz[5], Philipp J. Thurner[1], Alessandra Rossini[2] & Orestis G. Andriotis[1,6✉]

Mechanically characterizing biological tissues at the microscale helps to better link microscale biomechanics to mechanobiology but also contributes to the mechanistic understanding of disease mechanobiology. Cell spheroids (CSs) are state-of-the-art in vitro three-dimensional cell cultures allowing for the synthesis of microtissue models into sphere-like geometry. Such a geometry is attractive for micromechanical assessment via parallel-plate compression, since only minimal and nondestructive sample preparation is required to conduct such tests. However, appropriate data analysis and interpretation methods are mostly lacking. Current approaches, relying on Hertzian theory and its modifications, are inadequate for capturing large deformations observed in CSs upon compression. Here, we utilized the extended Tatara model, incorporating hyperelasticity and nonlinear boundary effects, to investigate CS mechanics. To evaluate the effectiveness of the model, we compared results to Hertz, Ding, and simple Tatara models. The extended Tatara model demonstrated superior accuracy, enabling mechanical analysis of CSs under compression of up to 50% strain. Estimating the apparent Poisson's ratio via image segmentation and shape analysis helped refine the calculated apparent modulus. This work establishes a robust analytical framework that will, in the future, help advance our understanding of cardiac fibrosis progression and support the development of therapeutic strategies using patient-derived CSs as test models.

Cells actively sense and respond to mechanical cues of their surrounding mechanical microenvironment provided by the extracellular matrix (ECM) and neighboring cells. Mechanical cues, such as compressive forces, apparent ECM stiffness, that is its elastic and viscous properties, play a pivotal role in triggering cellular processes, in health and disease, such as proliferation[1], differentiation[2], migration[3], apoptosis[4] and tissue remodeling[2]. Alteration in ECM mechanical properties is a hallmark of various fibrotic conditions such as cardiac fibrosis[5] and lung fibrosis[6]. In such pathological processes, not only do cells alter the mechanics of their ECM microenvironment but change their contractility[7,8] as a response to matrix stiffening. This leads to an altered mechano-homeostatic state, compared to the healthy situation[6]. Dysregulation of ECM mechano-homeostasis is not solely a consequence of pathology but may also be a reason for disease progression[9,10]. To understand the role of mechanobiological changes for the onset and progression of cardiac fibrosis, it is therefore important to mechanically characterize the fibrotic niche at the microscale.

In vivo, biological tissues, depending on their function, are subjected to various mechanical forces, such as compressive, tensile, or shear[11]. Soft biological tissues exhibit low stiffness, ranging from tens of pascals to several megapascals[12–14], and can therefore undergo large deformations under relatively low external forces. Nevertheless, the level of strain soft tissues typically experience is contingent upon both the physiological context and the specific tissue type. For instance, the heart tissue can be exposed to strains of 20%–30%[15] under physiological conditions, while in pathological conditions, e.g. arrhythmias, up to 80% strains[16]. It is therefore necessary to consider the relevance of large strains to tissue biomechanics and mechanobiology.

Classically, cell mechanics have been well documented using in vitro two-dimensional (2D) cell cultures. Although 2D systems have been an invaluable biological readout model, they do not account for extracellular barriers and 3D structure present in most in vivo[17,18] cases. The advent of 3D cell cultures, such as spheroids, has

[1]Institute of Lightweight Design and Structural Biomechanics, TU Wien, Vienna, Austria. [2]Institute for Biomedicine, Eurac Research, Bolzano, Italy. [3]Department of Neurosciences, Psychology, Drug Research & Child Health, University of Florence, Florence, Italy. [4]Institute of Materials Science and Technology, TU Wien, Vienna, Austria. [5]Institute of Applied Physics, TU Wien, Vienna, Austria. [6]Institute of Lightweight Design and Structural Biomechanics, Gumpendorfer Strasse 7, 1060 Vienna, Austria. ✉email: oandriot@ilsb.tuwien.ac.at

not only changed this but also enabled studying how cell–cell and cell–ECM interactions affect tissue mechanics under large physiological strain. As mentioned above, such 3D models mimic important aspects of the natural cellular microenvironment[19,20]. Several techniques have been employed for the mechanical assessment of cell spheroids (CSs), including parallel plate compression[21,22], atomic force microscopy (AFM)[23], micropipette aspiration[24], and microtweezers[25,26]. Among these, parallel-plate compression stands out as a straightforward method to assess the bulk properties requiring only minimal sample attachment[27–29].

With parallel-plate (and AFM-based) compression of CSs, contact mechanics models are employed to compute their apparent elasticity. While the Hertzian theory and its modifications (e.g., Johnson-Kendall-Roberts, Sneddon) are most typically used[23,30–33], they are derived upon the assumptions of small deformations and linear elastic behavior. However, CSs exhibit both material non-linearities, and, during parallel-plate compression, geometrical non-linearities (large deformations). This makes the Hertz theory inadequate for data analysis of CSs[34], especially under compression at large strains. Although some studies used models that consider hyperelasticity[22,35,36], none can so far describe the mechanics of CSs up to 50% apparent strain, which is in the physiological range for some soft tissues[37] (e.g. skin). Therefore, a model that combines both material and geometrical nonlinearities alongside a standardized methodology is direly needed to better describe, assess and compare the intricate mechanical behavior of CSs under compression.

To this end, we employed the extended Tatara model[38], which is a modified contact mechanics model employing a Mooney-Rivlin hyperelastic constitutive material behavior and is designed to specifically address shortcomings of the state-of-the-art Hertz and Ding models. In particular, the extended Tatara model considers material non-linearities and the change in contact area due to lateral extension, induced by the large compressive deformation. To evaluate the extended Tatara model, we compared its performance to three other models: the two most widely used models (a) Hertz and (b) Ding, and to (c) a simpler Tatara model (the latter only accounts for hyperelasticity and not for geometrical nonlinearities).

Results and discussion

Briefly, CSs were derived via a scaffold-free 3D approach by culturing human primary cardiac fibroblasts (hpCFs) (Fig. 1a). Of note, hpCFs, under physiological conditions, give structural support to the heart by regulating the synthesis and degradation of ECM proteins[5]. Subsequently, CSs were compressed individually at increasing speeds (Fig. 1b, c) up to 50% uniaxial strain with simultaneous tracking of the lateral deformation. Loading curves were fitted to the extended Tatara Model and results were compared to those similarly obtained by utilizing Hertz, Ding's, and Tatara's contact mechanics models (Fig. 1d). Additionally, by simultaneous tracking the CS lateral deformation, we estimated the apparent Poisson's ratio and, based on this, modified the assumption of incompressibility of the model, which affects the magnitude of the apparent modulus.

Origin of non-linear elasticity in cell spheroids

CSs were subjected to parallel-plate compression tests to up to 50% strain (whereby strain or compressive strain here and throughout the manuscript refers to apparent strain based on initial CS height). CSs exhibited a nonlinear increase of force vs. strain (right subplot of Fig. 1c) under compression, as a result of material, geometrical, and boundary non-linearities. On the one hand, the contact area of a CS under compression increases nonlinearly with strain. This increase is depicted in Fig. 1e, where the contact area is estimated based on two contact mechanics models: (i) the Hertzian (small strain and linear elasticity) theory and (ii) the extended Tatara (large strain and hyperelasticity) model. At small apparent strains (up to about 10%; Fig. 1e), the contact area predictions from both models coincide, while at larger strains (> 10%), they increasingly differ (grey area), due to the lateral expansion and the non-linear material behavior that only the extended Tatara model accounts for. On the other hand, cells[39], and ECM structural components, specifically collagen[40], are well known for their nonlinear mechanical properties that are expected to contribute to the overall nonlinear mechanics of the CS.

To better inspect the force vs. strain nonlinearity, the data are presented in a log-log plot (inset of right subplot in Fig. 1c) along with straight lines representing selected power-law $F–\varepsilon^n$ relationships. Up to 10% strain, the $F–\varepsilon^n$ curve conforms to the predictions of Hertzian theory (i.e., $F \propto \varepsilon_z^{3/2}$) indicating that elastic response dominates small strain deformation, and CSs behave similarly to a homogeneous, isotropic elastic material. However, from 10% to 45% strain, the behavior deviates from the Hertzian prediction, transitioning to a $F \propto \varepsilon^3$ power-law relationship, and subsequently, to a stiffer behavior, approaching $F \propto \varepsilon^5$, from 40% and up to 50% strain. This multifaceted power-law response was previously also observed in the compression of rubber spheres as described by Shima et al.[41].

Beyond the regime that can be analyzed assuming linear elastic behavior and small strains (Hertz theory), the CS microstructure undergoes considerable deformation-induced changes, involving deformation mechanisms of cellular and ECM components, leading to the non-linear force-strain relationship. The subsequent shift to a steeper power-law relationship at higher CS strains is indicative of permanent deformation (see paragraph 3 from Limitations and perspectives section) and/or compaction at the cellular level. It becomes apparent that the CS undergoes complex structural changes, which very likely also entail irreversible processes.

F-ε_z curve modeling

Microcompression is widely employed as the state-of-the-art method to mechanically characterize biomaterials, tissue components and biological systems at the microscale[42–44]. Some studies have employed a continuum mechanics approach[6,42,45] while others used contact mechanics models[46–48] to estimate a "modulus of elasticity", where it seems obvious, given the nonlinear behaviour of samples investigated, such a unique material property does not exist. Rather, this should be considered an apparent modulus that depends on loading case and displacement or force rate. To investigate the effect of displacement rate, we have compressed our CSs at 0.5, 1,
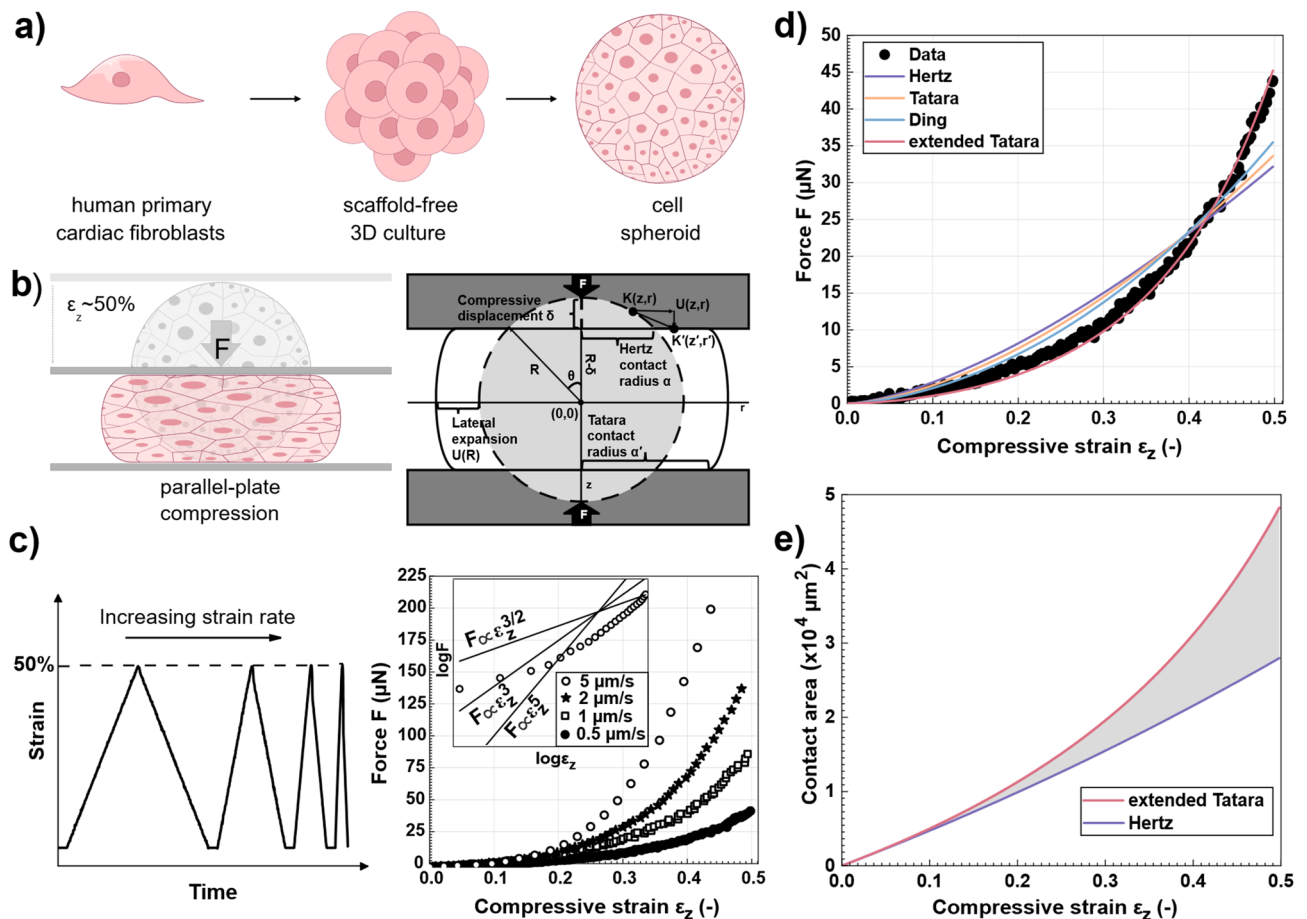
Fig. 1. (**a**) Schematic of CSs preparation. (**b**) 2D diagram of a CS compressed between two flat rigid plates which describes the interconnections between the extended Tatara model variables. (**c**) Force-strain data of a CS compressed up to 50% strain at four increasing displacement rates (0.5, 1, 2 and 5 μm/s). The inset in log-log scale shows the transition from Hertzian behavior, at small deformations, to approximately $F \propto \varepsilon^5$ at 50% strain. (**d**) Force-strain data of a CS compressed up to 50% strain at 0.5 μm/s displacement rate with the best-fitted curves obtained by fitting four contact mechanics models and, (**e**) and the corresponding contact area predicted by Hertz and the extended Tatara model as a function of compressive strain.

2, 5 μm/s. We evaluated the performance of four contact mechanics models; (a) Hertz, (b) Ding[49], (c) Tatara and (d) extended Tatara, assuming an apparent Poisson's ratio of 0.5[50]. The coefficient of determination (R^2; Fig. 2a, b) was calculated based on a least-squares fit of the applied forces utilizing experimental data within the 10–50% strain range. All models were subsequently fitted at 2.5% strain intervals within this strain range (Figure S1). Figure 2a and b show R^2 values as a function of maximum strain fitted (ε_{max_fitted}) at displacements rates 0.5 μm/s and 5 μm/s, respectively. The goodness of fit for each model was further assessed using the chi-squared (χ^2) statistical test. The resulting χ^2 values were normalized by the corresponding critical chi-squared (χ^2_{cr}) to obtain the normalized chi-squared (χ^2_{nrm}). Figure 2c and d show the comparison of χ^2_{nrm} values obtained by fitting the four models at 2.5% strain intervals within 10–50% strain range at displacements rates 0.5 μm/s and 5 μm/s, respectively. A value of χ^2_{nrm} less than 1 indicates that the fit passes (green color scale) the statistical test at 0.05 significance level, while values greater than 1 suggest that the model does not adequately describe the experimental data within the tested strain range (orange color scale).

At 0.5 μm/s displacement rate, R^2 increases from 0.85, at 10% strain, to 0.99, at 25% strain. R^2 values and their increasing trend with strain, at < 25%, are similar among all four models, however the Hertz model slightly outperforms Ding, Tatara, and extended Tatara. This can also be confirmed from Fig. 2c, where χ^2_{nrm} values obtained by fitting the Hertz model are smaller compared to the ones obtained by fitting the other models for the same fitting range. Fitting the Hertz model up to 27.5% strain returns the highest R^2 (Fig. 2a), which then drops faster, when fitting the data above 27.5% strain, compared to the Ding, Tatara, and extended Tatara. While Ding best fits the data from 30% to 40% strain, according to χ^2_{nrm} results (Fig. 2c), only the extended Tatara outperforms all models at strains higher than 40% and up to 50% strain. The improvement of Ding and Tatara can be attributed to the, respectively, neo-Hookean and Mooney-Rivlin material laws and the correction factor upon which these models are built. However, the extended Tatara provides a better fit at larger deformations, integrating both a hyperelastic material law (Mooney-Rivlin) and a large deformation formulation (accounting for contact area changes due to lateral expansion).
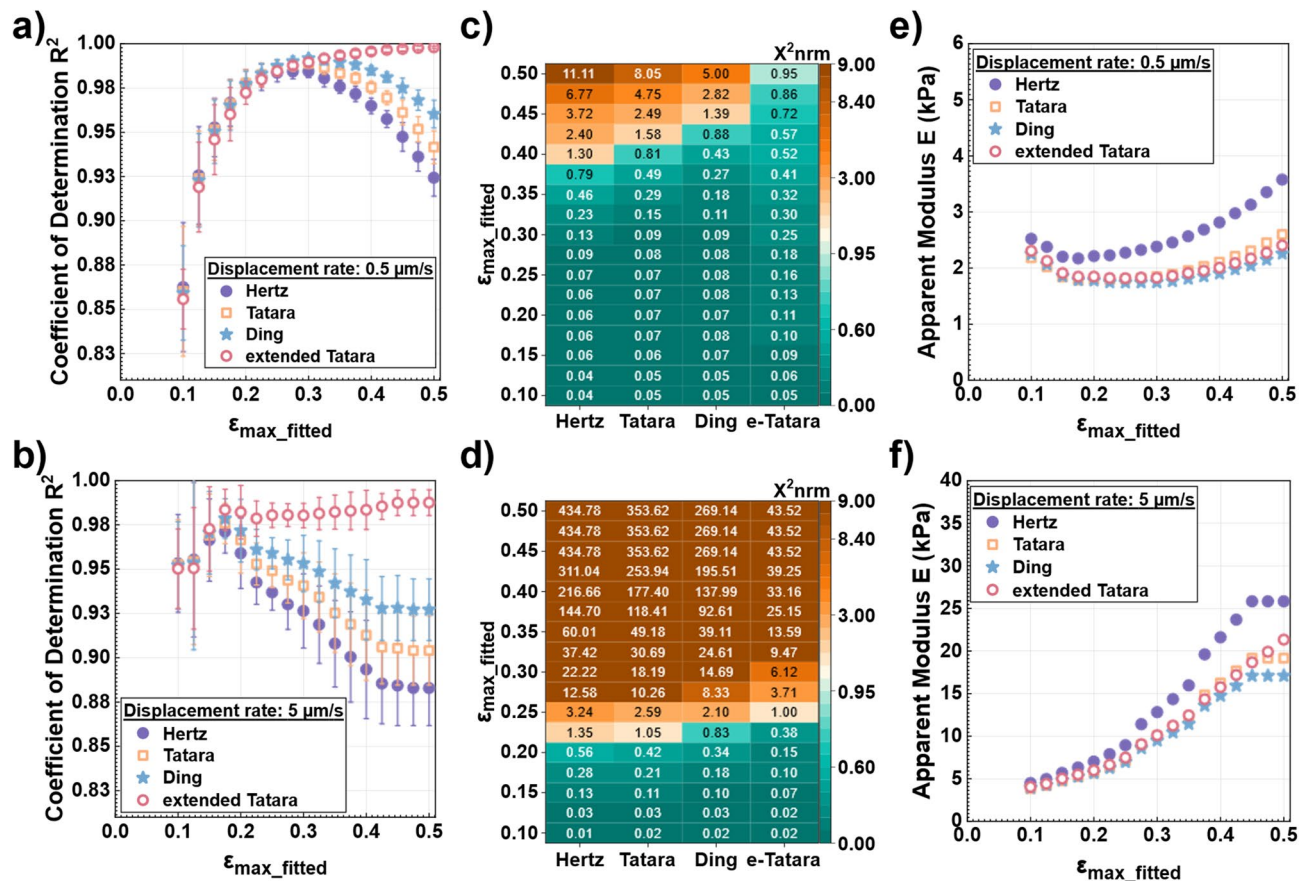
Fig. 2. Five CSs were compressed at displacement rates of 0.5 μm/s and 5 μm/s. The resulting F-ε_z data were fitted using four contact mechanics models at 2.5% strain intervals within the 10%–50% strain range. Panels show: R^2 values at displacement rates of (**a**) 0.5 μm/s and (**b**) 5 μm/s; χ^2 nrm values for one representative CS at (**c**) 0.5 μm/s and (**d**) 5 μm/s; and the corresponding apparent modulus values at (**e**) 0.5 μm/s and (**f**) 5 μm/s.

At 5 μm/s displacement rate, a similar trend in R^2 is observed for the Hertz, Ding and Tatara models, with all three reaching a peak at 17.5% strain. Interestingly, the Hertz, Ding and Tatara models exhibit a decline in R^2 between 20% and 42.5% strain, followed by a plateau until 50% strain. This trend is further supported by χ^2_{nrm} results (Fig. 2d), which indicate that the Hertz, Ding and Tatara models fail the χ^2 statistical test for strains beyond approximately 20%. The observed plateau hints to saturation (at 42.5% strain) beyond which these models can no longer account for the increase in contact area as a result of lateral expansion. In contrast, while the R^2 values from the extended Tatara model progressively increase when fitting the model up to 50% strain, the χ^2_{nrm} results (Fig. 2d) suggest that at a displacement rate of 5 μm/s this model is only adequately capturing the experimental data for strains up to approximately 25%.

Apparent modulus vs. maximum strain fitted relationship

The apparent modulus, calculated by fitting the force-displacement data using four contact mechanics models at different strain levels and displacement speeds of 0.5 μm/s and 5 μm/s, is shown in Fig. 2e and f, respectively. Qualitatively, the apparent modulus changes similarly among all four models with relation to the maximum strain fitted. However, the Hertz model consistently overestimates the apparent modulus at both 0.5 μm/s and 5 μm/s displacement rates, especially at higher strains. This overestimation is due to the Hertzian theory's limitation in considering the intricacies of non-linear deformations. Quantitatively, the apparent modulus calculated by all four models ranges from 1.5 kPa to 37 kPa.

At 0.5 μm/s displacement rate (Fig. 2e), the apparent modulus vs. strain fitted exhibits three distinct phases as strain increases. Initially, the apparent modulus, as predicted by all four models, decreases with increasing strain up to 17%. This behavior aligns with that observed in compressed foams, as reported by Bhagavathula et al.[51]. In their study on polymeric foams, a decrease in tangent modulus was observed at low strains, followed by an increase at higher strain levels, with the transition point varying depending on the strain rate. Similarly, Sun et al. noted a decrease in the unloading modulus when compressing various types of closed-cell foams, attributing the low stiffness at small strains (< 10%) to premature local yielding of the cell walls[52]. A CS is structurally composed of the ECM network and cells. With the above in mind and the results obtained from Fig. 3h, the initial decrease of the apparent modulus from 2.52 kPa to 2.17 kPa (from 10% to 17% strain) could be attributed to the local yielding of the ECM and cell cytoskeleton close to the surface of the cell spheroid. An additional contributing
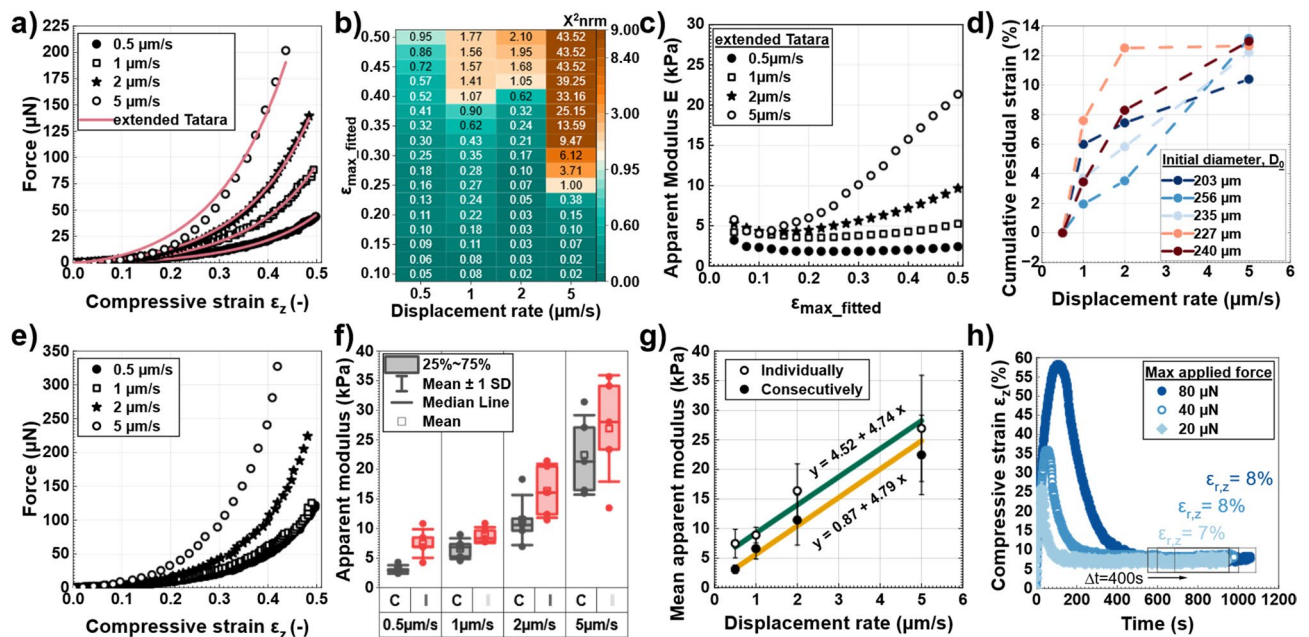
Fig. 3. (**a**) F-ε_z data of a CS compressed consecutively up to 50% strain at increasing displacement rates of 0.5, 1, 2, and 5 µm/s, with sample curves fitted using the extended Tatara model. (**b**) The corresponding χ^2_{nrm} values and, (**c**) apparent modulus obtained from the same fits. (**d**) Cumulative residual strain of the five CSs assessed due to consecutive compression. (**e**) F-ε_z data of four CSs compressed up to 50% strain at different displacement rates (0.5, 1, 2, and 5 µm/s). (**f**) Apparent modulus obtained from two groups: five CSs compressed consecutively at increasing displacement rates (C, grey boxplots), and twenty individual CSs (five per displacement rate) each compressed once up to 50% strain at 0.5, 1, 2, or 5 µm/s (I, red boxplots). (**g**) Mean apparent modulus of CSs compressed consecutively and individually at each displacement rate. (**h**) Three CSs loaded to maximum forces of 20, 40, and 80 µN at a rate of 1 µN/s, followed by unloading at the same rate. Residual strain was recorded over a 900 s duration of rest.

factor to the decreasing modulus at maximum strains fitted between 10% and 20% could be the low signal-to-noise ratio, shown in Figure S1a. At 10% fitted strains, the signal-to-noise ratio is low, forcing the model to be fitted with a higher slope compared to when fitted at 15% and 20% maximum strains.

Between 17% and 30% strain, the apparent modulus predicted by Ding and Tatara models enters a plateau phase, indicating a stable hyperelastic response. During this phase, the material maintains consistent stiffness despite increasing strain, a behavior not observed in the case of the Hertz model. Beyond 30% strain, the increasing apparent modulus may result from two deformation mechanisms; (a) structural densification of cells and, (b) strain stiffening of collagen. Previously, cell packing has been reported to be analogous to the packing of cellular structures of foams[53,54]. Rahimidehgolan and Altenhof reported a nonlinear increase of the stress-strain response in polymeric foams under uniaxial compression as a result of structural compaction, leading to stiffening[55]. In addition, collagen fibrils upon tension exhibit strain stiffening behavior[40]. Because CSs in this study are composed of both collagen (Picrosirius red staining, Fig. 4d) and cells (BioTracker and Hoechst 33342 staining, Fig. 4d), we expect both deformation mechanisms to be present.

At 5 µm/s displacement rate (Fig. 2f), the apparent modulus is constantly increasing up to 42.5% strain and then reaches a plateau because of model saturation (see paragraph 3 from F-ε_z curve modeling section). Unexpectedly, no initial decrease in apparent modulus due to boundary nonlinearities and surface heterogeneities was observed. This is likely because the CS has already been compressed at 0.5, 1 and 2 µm/s, resulting in an already densely packed structure. However, in some cases (Figure S2), the first phase was apparent, indicating variability between samples possibly due to material heterogeneity.

Effect of displacement rate

Compression tests of CSs were conducted at four displacement rates (0.5, 1, 2 and 5 µm/s) and the experimental F-ε_z data were fitted with the extended Tatara model as it is shown in Fig. 3a. The displacement rate-dependent nature of CSs is exhibited by the progressive increase of the F-ε_z curve slope with increasing displacement rate. Notably, the extended Tatara model performs better for displacement rates below 5 µm/s. The displacement rate dependency of the mechanical response can be attributed to the combined elastic, viscous and plastic mechanical behavior of both cells[39,56] and ECM components[1]. A similar trend is observed with the Hertz model and its extensions, where the effect of the displacement rate is more apparent (Fig. 2a, b). In general, R^2 values at 0.5 µm/s displacement rate are higher than those at 5 µm/s displacement rate for the same strains (Fig. 2a and b). However, the opposite trend is observed at low strains, which can be attributed to the scatter in the initial part of the curve (see paragraph 1 from Limitations and Perspectives section).
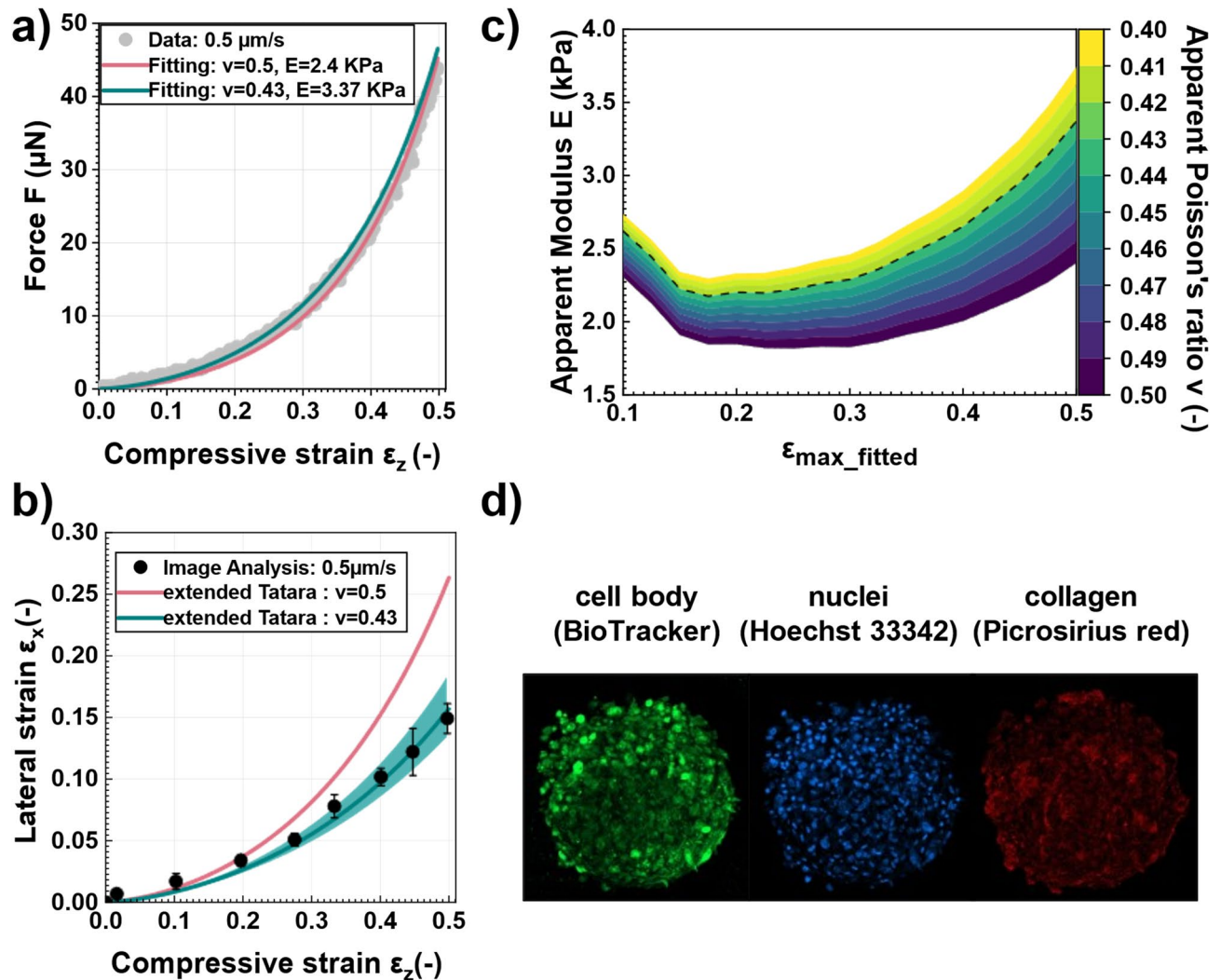
Fig. 4. (**a**) F-ε_z fitting before (red) and after (green) apparent Poisson's ratio correction. (**b**) Lateral strain ε_x as a function of compressive strain ε_z. The red and green curves represent the computed lateral strain assuming incompressibility and compressibility, respectively. The black dots were obtained from the CS image segmentation and shape analysis. Error bars represent standard deviation ($n = 6$), (**c**) Sensitivity of the apparent modulus calculated at 0.5 µm/s displacement rate to variations in apparent Poisson's ratio, (**d**) Confocal fluorescence images of a CS composed of human primary cardiac fibroblasts, stained with BioTracker 488 (cell body, green), Hoechst 33342 (cell nuclei, blue) and Picrosirius red (collagen fibrils, red). Showing a maximum intensity projection of a 70 µm z-stack.

The goodness of fit at the different displacements rates was further assessed using the χ^2 statistical test. Figure 3b shows the χ^2_{nrm} values obtained by fitting the extended Tatara model at 2.5% strain intervals within 10%–50% strain range at displacements rates 0.5, 1, 2 and 5 µm/s. The observation that the extended Tatara model performs better at lower displacement rates is further supported by the χ^2 statistical test. The extended Tatara model passes the χ^2 statistical test across the entire fitted range at 0.5 µm/s displacement rate, but only adequately captures the experimental data up to approximately 40% strain at 1 µm/s and 2 µm/s, and up to 25% strain at 5 µm/s.

Figure 3c shows the evolution of the strain-dependent apparent modulus (Eq. 11) obtained by fitting the extended Tatara model to the F-ε_z data with increasing strain at different displacement rates. At 0.5 µm/s displacement rate, the apparent modulus values are more consistent compared to the ones calculated at higher displacement rates. This indicates that the extended Tatara model predicts a similar apparent modulus regardless of the fitting range. The magnitude of apparent modulus increases along with the increasing applied displacement rate. The apparent modulus increases faster with compressive strain at higher applied displacement rates. This behavior was observed in all tested CSs (Figure S2). It is, therefore, essential to specify the fitting range, i.e., compressive strain, and displacement rates when reporting apparent modulus values.

The performance of all four contact models at lower displacement rates can be attributed to the viscous nature of CSs. Slower compression rates allow more time for stress relaxation, enabling the viscous and other transient components of the mechanical response to dissipate. Consequently, the measured data at lower displacement

rates predominantly reflect a hyperelastic response, which is better captured by the contact models. However, permanent deformation can contribute to the observed displacement-rate dependency. Since the same CSs were consecutively compressed up to 50% strain at increasing displacement rates of 0.5, 1, 2, and 5 μm/s, residual strain may accumulate, influencing both the mechanical response of the CSs and the corresponding apparent modulus values. Figure 3d shows the cumulative residual strain of the five CSs used in this study, along with their initial diameters. The method used to calculate both cumulative residual strain and initial diameters is detailed in Figure S3. Figure 3d shows that residual strain accumulates between successive loading/unloading cycles, reaching approximately 12% prior to the final loading at 5 μm/s. This is a considerable value relative to the total applied strain and may affect the accuracy of the apparent modulus values obtained at higher displacement rates.

To test whether the increase in apparent modulus with increasing displacement rate is solely due to the viscous response of the CSs or influenced by both viscous effects and residual strain, in total twenty individual CSs (five per displacement rate) were each compressed once up to about 50% strain at 0.5, 1, 2, or 5 μm/s. Figure 3e shows representative F-ε_z curves of four CSs compressed up to 50% strain at different displacement rates of 0.5, 1, 2, and 5 μm/s. A progressive increase in the slope of the F-ε_z curves with increasing displacement rate is observed, similar to the behavior seen when CSs were compressed consecutively (Fig. 3a). The F-ε_z data were fitted with the extended Tatara model and the apparent modulus of the twenty CSs was calculated (Eq. 11). Figure 3f shows a comparison of the apparent modulus between the CSs compressed consecutively (group C, grey boxplots) and the twenty individual CSs compressed once (group I, red boxplots) at 0.5, 1, 2, or 5 displacement rate μm/s. Interestingly, the increase in apparent modulus with displacement rate in the individual tests is almost identical to the increase observed in the consecutive loading tests, as evident from the slope shown in Fig. 3g. Notably, the apparent modulus of CSs tested individually (I) at different displacement rates is overall higher (Fig. 3f; red boxplots) than that of CSs tested consecutively (C; Fig. 3f; gray boxplots). We attribute this difference to the inherent heterogeneity between donors, as the individual tests (red boxplots) were conducted on CSs derived from a different donor than those used in the consecutive tests (gray boxplots). Additionally, to quantify the residual strain as a proxy for permanent deformation, we conducted loading-unloading-holding tests (Fig. 3h). Three different CSs were compressed to maximum forces of 20 μN, 40 μN and 80 μN at 1 μN/s loading rate, and then unloaded at the same rate, followed by a holding phase of up to 15 min. During the holding phase, the force was kept constant at 0.5 uN, equal to the preload applied before the loading phase. Figure 3h shows the resulting compressive strain over time. The residual strain ranges between 7% and 8%, which is relatively low compared to the overall applied strains of 26%, 36% and 58%. Taken together, these findings indicate that although permanent deformation is present, it does not have a substantial impact on the estimation of the apparent modulus. Therefore, the observed rate dependency is primarily due to the elastic and viscous response.

Apparent modulus correction via geometrical analysis

The apparent modulus estimation necessitates the assumption of a specific value for apparent Poisson's ratio (ν). Some studies assume incompressibility (ν = 0.5)[57], while others observed a volumetric change (ν < 0.5)[58–61]. Therefore, a precise determination of the apparent Poisson's ratio is necessary for obtaining an accurate apparent modulus[50,62].

The apparent modulus values presented in Fig. 2e and f were computed, assuming incompressibility, i.e., *ν = 0.5*. As an example, fitting the extended Tatara model to the F-ε_z curve up to 50% strain, assuming ν = 0.5, predicts an apparent modulus of 2.40 kPa (red, Fig. 4a) and a lateral strain at the horizontal diameter at *z = R* of 0.26 (red, Fig. 4b). Applying image segmentation and shape analysis (Figure S4) on images recorded during the compression of CSs, we measured the experimental lateral strain (black dots, *n* = 6, Fig. 4b). While the extended Tatara model performs a good fit (R² > 0.99) with the F-ε_z curve over the entire range, it overestimates the measured lateral strain for compressive strains beyond 20% (ε_z < 0.2), indicating compressibility (Fig. 4a). Utilizing explicit numerical relationships (Eq. 23 and Eq. 24, Figure S5), we estimated an apparent Poisson's ratio of 0.43, and consequently, the predicted lateral strain is in good agreement with the measured lateral strain (green, Fig. 4b). However, in the low strain regime (strain < 20%), the measured lateral strain is slightly underestimated by the extended Tatara model. This behavior was observed in all the CSs measured in this study (shaded area, Fig. 4b). Liu et al. observed a similar trend in the lateral strain of polyurethane spheres under compression[63]. Another possible explanation for this deviation at low strains can be the limitation in the force sensitivity of the cantilever (see paragraph 1 from Limitations and perspectives section). Finally, fitting the extended Tatara model to the F-ε_z data assuming apparent Poisson's ratio of 0.43, an apparent modulus of 3.37 kPa was computed (green, Fig. 4a). The good fit of the extended Tatara model (R² > 0.99) for both apparent Poisson's ratios indicates that the model is robust in capturing the force-strain relationship of the data. The 40% increase in apparent modulus due to a change in apparent Poisson's ratio from 0.5 to 0.43 underscores the importance of determining lateral expansion of the sample. We further assessed the influence of apparent Poisson's ratio on the measured apparent modulus values. As shown in Fig. 4c, the apparent modulus increases with decreasing apparent Poisson's ratio and its effect on calculated apparent modulus values becomes larger at higher compressive strains.

Limitations and perspectives

During the compression tests, we experienced experimental noise in the initial stages of contact, which is most likely responsible for the low performance (R² < 0.95) of all contact models up to 15% strain. Although a preload of 0.5 μN was applied to the CS, the initial part of the F-ε_z curve is accompanied with more noise compared to the force resolution and sensitivity of the cantilever used. The cantilever used has an estimated stiffness of 0.55 N/m and a force resolution of about 0.6 μN. A stiffer cantilever (i.e., of 2.4 N/m available from the manufacturer) offers lower force resolution, of about 3 μN, while a softer cantilever (of 0.15 N/m) offers higher force resolution of about 0.2 μN. Given these choices, the cantilever used here offers the highest possible measurement sensitivity throughout the whole force range of the tests (25 μN – 300 μN, Figure S6). Briefly, a cantilever too stiff, will have

small deflection and high noise, while a cantilever too soft will deflect without transmitting any compression to the sample. Force measurement sensitivity is optimal when sample and cantilever stiffnesses are well-matched. The ratio of cantilever deflection vs. base displacement (of the cantilever) provides a good estimate of the measurement sensitivity in cantilever-based force sensors[64,65]. The trade-off in cantilever stiffness necessitated choosing a cantilever capable of measuring the full range of forces applied with sufficient signal-to-noise ratio.

The extended Tatara model is built upon the constant volume and Poisson's ratio assumptions. Furthermore, CSs are treated as spheres for volume calculations, which may not represent the true shape and volume. Five CSs were assessed, and in every case, image segmentation and shape analysis revealed a volume decrease of 2%–4.5% after compression to 50% strain, compared to the initial volume before loading. CSs are composed of cells, ECM and interstitial fluid[66]. These components have different material properties and are not homogenously distributed across the CS volume (spatial heterogeneity of structural components), which further adds to the complexity of CS mechanical behavior (Fig. 4d).

The model employed in this study assumes hyperelastic behavior, which constitutes a limitation. Our findings demonstrate that the mechanical response of CSs is displacement rate-dependent, due to the presence of viscoelastic effects, and, to a lesser extent, of permanent deformation. Consequently, the proposed model is not equipped to capture the time-dependent viscous behavior of CSs (or permanent deformation).

As a perspective, based on the results obtained in this study, several methodological improvements are proposed to enhance the accuracy of measuring and analyzing CSs. It is advisable to limit compression to 30% strain to prevent the onset of permanent deformations, which could compromise the validity of the results. Furthermore, it is crucial to integrate the actual geometry of the samples into the contact model, as the current approach assumes spherical symmetry, which may not accurately represent the true shape of the CSs. Lastly, conducting a comprehensive geometrical analysis to better determine the apparent Poisson's ratio of the samples would provide a more precise characterization of their mechanical behavior, leading to improved agreement between experimental observations and theoretical models.

Conclusions

Here, we utilized a contact mechanics model—namely the extended Tatara model—to mechanically characterize CSs under large compressive deformations. We additionally report the shortcomings of using the Hertz, Ding and Tatara model (the latter not to be confused with the extended Tatara model) in accurately estimating the stiffness of CSs. The limitations of these three models are addressed by the extended Tatara model because it is built upon two assumptions that are, in many cases, necessary for CS mechanical characterization: (a) large deformation to account for the change in contact area due to lateral stretching of the CS and (b) nonlinear material behavior that considers the nonlinear mechanical properties of the structural components of CSs. Interestingly, by comparing the measured lateral strain, obtained from image analysis, with the prediction from the extended Tatara model, a correction for the apparent Poisson's ratio was also needed to provide a better description of the deformation and thus CS measured stiffness. We envisage that such an improved analysis might provide a more accurate approach in determining the mechanical properties of CSs; this observation is of particular relevance in light of crucial mechanical cues, such as changes in mechanical properties integral to cell processes in health and disease.

Methods
Cell spheroids Preparation

Cardiac fibroblasts were obtained as outgrowths from surgical heart biopsy tissue from patients diagnosed with Hypertrophic Cardiomyopathy (HCM), as previously described[67]. The fibroblasts (1.5×10^6 per well) were seeded in AggreWell™800 Plates, pretreated with anti-adherence rinsing solution in Iscove's Modified Dulbecco's Medium (IMDM) containing 20% Fetal Bovine Serum (FBS), 1% Glutamine, 1% Pen/Strep and 10 ng/ml basic fibroblast growth factor (bFGF). Each well contains a standardized array of microwells 800 μm in size. The CSs were cultured for two days, frozen and stored at −80 °C until parallel-plate compression testing. The study was approved by the Ethical Committee of the Province of Alto Adige/South Tyrol (Nr. 5/2018) and the Regional Ethical Committee for the clinical experimentation of Tuscany (Nr. 19337_bio) and it conformed to the ethical guidelines of the declaration of Helsinki. All patients provided written informed consent.

Parallel-plate compression testing

In total, five CSs were mechanically assessed (on the same day) via parallel-plate compression using the CellScale MicroSquisher (CellScale, Ontario, Canada) and the corresponding SquisherJoy software. CSs were thawed and placed into the fluid bath test chamber (filled with sterile phosphate buffered saline (PBS) pH 7.4) in which parallel-plate compression took place. Each CS was compressed by a square stainless-steel flat plate fixed at the end of a 6 cm round tungsten cantilever with 0.2032 mm diameter. The cantilever was chosen based on the required force sensitivity (0.6 μN), while the stage and cameras were calibrated according to manufacturer's instructions. CSs were compressed up to 50% apparent linear strain at subsequent displacement rates of 0.5, 1, 2, and 5 μm/s, and released back to the original position (unloading speed) always using the same displacement rate. To calculate the apparent modulus, force and displacement data were fitted with four contact mechanics models that were implemented, namely, Hertz, Tatara, Ding, extended Tatara, in a custom MATLAB script (v. R2023a, MathWorks, Natick, MA, USA). The optimal apparent modulus was obtained for minimum error between the measured and predicted force values. The goodness of fit for each model was assessed using the coefficient of determination (R^2) and the chi-squared (χ^2) statistical test, performed with 95% confidence. For the χ^2 analysis, the uncertainty in force measurements was estimated by considering the resolution of the cantilever and the accuracy of the force transducer. Unless otherwise specified, apparent Poisson's ratio of 0.5 was assumed.

Contact mechanics theories for the F-ε_z curve modeling

To estimate the stiffness of the CSs, the force-displacement data was assessed by contact mechanics models. Table S1 summarizes the assumptions of the four contact mechanics models used in this study.

According to the elasticity theory, when an elastic half-space is subjected to a concentrated compressive force (F) along the z-axis, the vertical displacement (w) and radial displacement (u) can be described in cylindrical coordinates (z, r) as follows[68,69]:

$$w(z,r) = \frac{F}{2\pi E} \left(\frac{(1+\nu)z^2}{(r^2+z^2)^{3/2}} + \frac{2(1-\nu^2)}{(r^2+z^2)^{1/2}} \right) \tag{1}$$

$$u(z,r) = \frac{(1+\nu)F}{2\pi ER} \left(\frac{zr^2}{(r^2+z^2)^{3/2}} - (1-2\nu)\left(1 - \frac{z}{(r^2+z^2)^{1/2}}\right) \right) \tag{2}$$

where ν is the Poisson's ratio, R the radius of the sphere before compression and E is the apparent modulus of the sample.

Hertz model

For z = 0, Eq. (1) corresponds to the Hertzian solution. The Hertz model relies on the following assumptions: (i) the surface is an infinitely large half-space elastic body (area of contact is much smaller than the radius of the body), (ii) strains are small and limited within the elastic region, and (iii) surfaces are continuous and non-conforming. For an elastic sphere under parallel plate compression, the relationship between the force, F, and the displacement, δ, according to Hertz, is given by[70]:

$$F = \frac{4}{3}\sqrt{R}E'\delta^{3/2} \tag{3}$$

where δ is half the measured displacement D which represents the total CS displacement (the sum of the top and bottom deformations). The reduced modulus, E′, for a plate much stiffer than the sample ($E_{plate} \gg E$) is given by[71–73]:

$$E' = \frac{E}{1-\nu^2} \tag{4}$$

Tatara model

To address the non-half-space nature of compressing spheres, Tatara introduced the following relationship between the compressive displacement and force[74,75]:

$$\delta = \frac{3(1-\nu^2)F}{4E\alpha} - \frac{f(\alpha)F}{\pi E} \tag{5}$$

where α is the Hertzian contact radius and f(α) is given by:

$$f(a) = \frac{2(1+\nu)R^2}{(\alpha^2+4R^2)^{3/2}} + \frac{1-\nu^2}{(\alpha^2+4R^2)^{1/2}} \tag{6}$$

In Eq. (5), the first term corresponds to the Hertzian solution while the second term was introduced due to the reaction force acting on the opposite contact surface (z = 2R) to account for larger deformations. Equations (5) and (6) provide an implicit form of Tatara's model. The Hertzian contact radius is calculated geometrically as a function of the compressive displacement[76]. However, here, the following equation, adopted from Wang et al.[77], is used:

$$\frac{\alpha}{2R} = c_1\frac{\delta}{R} + 0.5\left(\frac{\delta}{R}\right)^{1/2} \tag{7}$$

where,

$$c_1 = -0.0151181\nu^2 - 0.012747\nu + 0.039931 \tag{8}$$

Ding model

When a CS undergoes notable deformation, the linear elastic assumption in the Hertzian theory cannot be considered valid. Ding addressed this assumption by taking into account the hyperelastic behavior of cells[49,78]. The model was derived numerically using the neo-Hookean constitutive law. According to the dimensional analysis, the correlation between the force and compressive displacement is given by[79]:

$$F = \frac{4}{3} E' \sqrt{R}\ \delta^{3/2} \prod_{nH}\left(\frac{\delta}{R}, \beta\right) \tag{9}$$

where Π_{nH} is a dimensionless function depending on the size ratio β (β = radius of indenter/radius of sample). For the case of an elastic sphere compressed by a rigid flat plate, Eq. (9) reduces to the following Eq. 8[80]:

$$F = \frac{4}{3} E' \sqrt{R}\ \delta^{3/2}\left(1 + 0.5\frac{\delta}{R}\right) \tag{10}$$

Extended Tatara model

Tatara extended his previous model[38] to account for even larger deformations considering the non-linear behavior of the material. Based on the Mooney–Rivlin hyperelastic material law, the strain-dependent apparent modulus is given as a function of the compressive strain ε_z by[38]:

$$E = E_0 \frac{1 - \epsilon_z + (\epsilon_z)^2/3}{(1 - \epsilon_z)^2} \tag{11}$$

where E_0 is the apparent modulus at $\varepsilon_z = 0$. At large strains, the change in shape due to deformations in the transverse direction cannot be neglected. Another benefit of this model is that it enables the calculation of this lateral expansion. The following set of constitutive equations provide an implicit form of Tatara's extended model[63]:

$$z = R - \left(R^2 - \alpha^2\right)^{1/2} \tag{12}$$

$$z = AF\left[\frac{3}{8E_0'\alpha}\left(1 - \frac{Ba^2}{2R^2}\right) + \frac{Bg(\alpha)\alpha^2}{2\pi R^2 E_0'}\right] \tag{13}$$

$$U(z,\alpha) = \frac{AF}{2\pi E_0'(1-\nu)}\left(1 + \frac{B\alpha^2}{5R^2}\right)\left(\frac{\sqrt{z} + (2R-z)^{1/2}}{2\sqrt{2}R^{3/2}} - \frac{(1-2\nu)\left[2(2R)^{1/2} - \sqrt{z} - (2R-z)^{1/2}\right]}{[2Rz(2R-z)]^{1/2}}\right) \tag{14}$$

$$U(R,\alpha) = \frac{AF}{\pi R E_0'(1-\nu)}\left(1 + \frac{B\alpha^2}{5R^2}\right)\left[\frac{\sqrt{2}}{4} - (1-2\nu)\left(1 - \frac{\sqrt{2}}{2}\right)\right] \tag{15}$$

$$\alpha' = \alpha + U(z,\alpha) \tag{16}$$

$$A = \frac{(1-\xi)^2}{1 - \xi + \xi^2/3} \tag{17}$$

$$B = \frac{1 - \xi/3}{1 - \xi + \xi^2/3} \tag{18}$$

$$\xi = \frac{\delta}{R} \tag{19}$$

$$g(a) = \frac{1}{\left(\alpha^2 + 4R^2\right)^{1/2}} + \frac{2R^2}{(1-\nu)\left(\alpha^2 + 4R^2\right)^{3/2}} \tag{20}$$

where U(z, α) is the lateral expansion at the vertical position z, U(R, α) is the lateral expansion at the horizontal diameter at z = R and α′ is the Tatara contact radius. Figure 1c depicts the geometrical interconnections among the aforementioned variables. The main drawback of this theory is that the governing equations cannot be solved analytically. To address the issue, an explicit relationship between the compressive displacement δ and the Hertzian contact radius α was used[77]:

$$\frac{\alpha}{2R} = d_1\left(\frac{\delta}{R}\right)^{3/2} + 0.5\left(\frac{\delta}{R}\right)^{1/2} \tag{21}$$

where,

$$d_1 = \frac{0.1787\nu - 0.07141}{\nu^3 - 0.6737\nu^2 - 0.8102\nu + 0.6045} \tag{22}$$

Cell spheroid image segmentation and shape analysis

The deformation of the CSs was captured through camera recordings and the data acquisition frequency was set to 1 Hz. Image analysis was performed on these image datasets using a custom MATLAB script. The script includes a series of preprocessing steps such as cropping, grayscale conversion, and manual thresholding, followed by morphological operations and the Canny edge detection algorithm to remove noise artifacts and isolate the object, respectively. The lateral expansion of the CS U(R, α) was estimated after boundaries identification by using a bounding box. The area and volume of the CS were measured by fitting an ellipse based on the dimensions of the bounding box. All the images were processed using consistent parameters. The step-by-step automated workflow for detecting and analyzing the CSs is depicted in Figure S4. To estimate the apparent Poisson's ratio of the CSs, an explicit numerical relationship was adopted from[63]:

For $U^*(R, \alpha) \geq 0.0485$

$$\nu\left(U^*(R, \alpha)\right) = 81.163\left(U^*(R, \alpha)\right)^3 - 38.535\left(U^*(R, \alpha)\right)^2 + 6.989\left(U^*(R, \alpha)\right) + 0.04242 \quad (23)$$

For $U^*(R, \alpha) < 0.0485$

$$\nu\left(U^*(R, \alpha)\right) = -126270\left(U^*(R, \alpha)\right)^4 + 12173\left(U^*(R, \alpha)\right)^3 - 473.2\left(U^*(R, \alpha)\right)^2 + 16.94\left(U^*(R, \alpha)\right) - 0.0984 \quad (24)$$

where $U^*(R, \alpha)$ is the dimensionless lateral expansion $(U(R, \alpha)/R)$ at the horizontal diameter at $z = R$ at 40% dimensionless approach ξ (Figure S5).

Cell spheroid staining and confocal microscopy

CSs were stained using cell body BioTracker green stain (Sigma-Aldrich, 5µM), Hoechst 33342 stain (Thermo Fisher Scientific, 10 µg/mL) and Picrosirius Red (Morphisto, 0.1% Sirius red in saturated picric acid), according to manufacturer's protocols. In short, live CSs were stained for 30 min with BioTracker green at 37 °C with 5% CO_2 incubation. Upon staining fresh medium was replenished twice to hydrolyze free dye. After a PBS wash, CSs were fixed with 4% formaldehyde for 30 min and permeabilized with 0.25% Triton X solution for 45 min at room temperature. After a subsequent wash, picrosirius red stain was applied for 2 h. Hoechst staining was added after washing out picrosirius-red for 30 min, followed by confocal imaging.

Confocal microscopy of CSs was carried out with a Zeiss LSM800 confocal microscope, using a plan-apochromat air x10, 0.45 NA objective (Zeiss), operated by ZEN blue software. Z-stacks of individual CSs were captured covering a 70 µm Z-range, with 5 µm offset between slices. Maximum intensity projections of the stacks (Fig. 4d) were obtained using ZEN blue software.

Data availability

The MATLAB scripts used for data and image analysis are available from the corresponding author on request.

References

1. Chaudhuri, O., Cooper-White, J., Janmey, P. A., Mooney, D. J. & Shenoy, V. B. Effects of extracellular matrix viscoelasticity on cellular behaviour. *Nature* **584**, 535–546 (2020).
2. Yamada, K. M., Doyle, A. D. & Lu, J. Cell–3D matrix interactions: recent advances and opportunities. *Trends Cell. Biol.* **32**, 883–895 (2022).
3. Janmey, P. A. & Fletcher, D. A. Reinhart-King, C. A. Stiffness sensing by cells. *Physiol. Rev.* **100**, 695–724 (2020).
4. Wang, H. B., Dembo, M. & Wang, Y. L. Substrate flexibility regulates growth and apoptosis of normal but not transformed cells. *Am. J. Physiol. - Cell. Physiol.* **279**, 1345–1350 (2000).
5. Schlittler, M., Pramstaller, P. P., Rossini, A. & De Bortoli, M. Myocardial fibrosis in hypertrophic cardiomyopathy: A perspective from fibroblasts. *Int. J. Mol. Sci.* **24**, 14845 (2023).
6. Jones, M. G. et al. Nanoscale dysregulation of collagen structure-function disrupts mechano-homeostasis and mediates pulmonary fibrosis. *Elife* **7**, 1–24 (2018).
7. Pakshir, P. et al. Dynamic fibroblast contractions attract remote macrophages in fibrillar collagen matrix. *Nat. Commun.* **10**, 1–17 (2019).
8. Discher, D. E., Janmey, P. & Wang, Y. L. Tissue cells feel and respond to the stiffness of their substrate. *Sci. (80-).* **310**, 1139–1143 (2005).
9. Herrera, J., Henke, C. A. & Bitterman, P. B. Extracellular matrix as a driver of progressive fibrosis. *J. Clin. Invest.* **128**, 45–53 (2018).
10. Saucerman, J. J., Tan, P. M., Buchholz, K. S., McCulloch, A. D. & Omens, J. H. Mechanical regulation of gene expression in cardiac myocytes and fibroblasts. *Nat. Rev. Cardiol.* **16**, 361–378 (2019).
11. Wang, J. H. & Li, B. Mechanics rules cell biology. *BMC Sports Sci. Med. Rehabil.* **2**, 16 (2010).
12. Guimarães, C. F., Gasperini, L., Marques, A. P. & Reis, R. L. The stiffness of living tissues and its implications for tissue engineering. *Nat. Rev. Mater.* **5**, 351–370 (2020).
13. Akhtar, R., Sherratt, M. J., Cruickshank, J. K. & Derby, B. Characterizing the elastic properties of tissues. *Mater. Today.* **14**, 96–105 (2011).
14. Efremov, Y. M., Okajima, T. & Raman, A. Measuring viscoelasticity of soft biological samples using atomic force microscopy. *Soft Matter.* **16**, 64–81 (2019).
15. Smiseth, O. A., Torp, H., Opdahl, A., Haugaa, K. H. & Urheim, S. Myocardial strain imaging: how useful is it in clinical decision making? *Eur. Heart J.* **37**, 1196–1207 (2016).
16. Weidemann, F. et al. Myocardial function defined by strain rate and strain during alterations in inotropic States and heart rate. *Am. J. Physiol. Circ. Physiol.* **283**, H792–H799 (2002).
17. Kapałczyńska, M. et al. 2D and 3D cell cultures – a comparison of different types of cancer cell cultures. *Arch. Med. Sci.* **14**, 910–919 (2016).
18. Poornima, K. et al. Implications of Three-Dimensional cell culture in Cancer therapeutic research. *Front. Oncol.* **12**, 1–12 (2022).

19. Kim, S., Kim, E. M., Yamamoto, M., Park, H. & Shin, H. Engineering Multi-Cellular spheroids for tissue engineering and regenerative medicine. *Adv. Healthc. Mater.* **9**, 2000608 (2020).

20. Zhao, Z. et al. Organoids. *Nat. Rev. Methods Prim.* **2**, 94 (2022).

21. Brodland, G. W., Yang, J. & Sweny, J. Cellular interfacial and surface tensions determined from aggregate compression tests using a finite element model. *HFSP J.* **3**, 273–281 (2009).

22. Giverso, C., Di Stefano, S., Grillo, A. & Preziosi, L. A three dimensional model of multicellular aggregate compression. *Soft Matter.* **15**, 10005–10019 (2019).

23. Vyas, V., Solomon, M., D'Souza, G. G. M. & Huey, B. D. Nanomechanical analysis of extracellular matrix and cells in multicellular spheroids. *Cell. Mol. Bioeng.* **12**, 203–214 (2019).

24. Sciumè, G., Guevorkian, K. & Nassoy, P. A bi-component model to assess the rheology of soft cellular aggregates probed using the micropipette aspiration technique. *Acta Biomater.* **189**, 449–460 (2024).

25. Dolega, M. et al. Mechanical behavior of multi-cellular spheroids under osmotic compression. *J. Mech. Phys. Solids.* **147**, 104205 (2021).

26. Boot, R. C. et al. High-throughput mechanophenotyping of multicellular spheroids using a microfluidic micropipette aspiration chip. *Lab. Chip.* **23**, 1768–1778 (2023).

27. Efremov, Y. M. et al. Mechanical properties of cell sheets and spheroids: the link between single cells and complex tissues. *Biophys. Rev.* **13**, 541–561 (2021).

28. Nakano, K., Nanri, N., Tsukamoto, Y. & Akashi, M. Mechanical activities of self-beating cardiomyocyte aggregates under mechanical compression. *Sci. Rep.* **11**, 1–10 (2021).

29. Navindaran, K., Kang, J. S. & Moon, K. Techniques for characterizing mechanical properties of soft tissues. *J. Mech. Behav. Biomed. Mater.* **138**, 105575 (2023).

30. Marturano, J. E., Arena, J. D., Schiller, Z. A., Georgakoudi, I. & Kuo, C. K. Characterization of mechanical and biochemical properties of developing embryonic tendon. *Proc. Natl. Acad. Sci. U S A.* **110**, 6370–6375 (2013).

31. Conrad, C., Gray, K. M., Stroka, K. M., Rizvi, I. & Scarcelli, G. Mechanical characterization of 3D ovarian Cancer nodules using Brillouin confocal microscopy. *Cell. Mol. Bioeng.* **12**, 215–226 (2019).

32. Chu, Y. S., Dufour, S., Thiery, J. P., Perez, E. & Pincet, F. Johnson-Kendall-Roberts theory applied to living cells. *Phys. Rev. Lett.* **94**, 1–4 (2005).

33. Hoehme, S. & Drasdo, D. Biomechanical and nutrient controls in the growth of mammalian cell populations. *Math. Popul. Stud.* **17**, 166–187 (2010).

34. Kontomaris, S. V., Malamou, A. & Stylianou, A. The Hertzian theory in AFM nanoindentation experiments regarding biological samples: overcoming limitations in data processing. *Micron* **155**, 103228 (2022).

35. Ding, Y., Niu, X. R. & Wang, G. F. Elastic compression of nanoparticles with surface energy. *J Phys. D Appl. Phys* **48**, (2015).

36. Efremov, Y. M. et al. Anisotropy vs isotropy in living cell indentation with AFM. *Sci. Rep.* **9**, 1–12 (2019).

37. Carnevale, A. et al. Skin strain analysis of the scapular region and wearables design. *Sensors* **21**, 5761 (2021).

38. Tatara, Y. Large deformations of a rubber sphere under diametral compression: part 1 : theoretical analysis of press approach, contact radius and lateral extension. *JSME Int. J. Ser. Mech. Mater. Eng.* **36**, 190–196 (1993).

39. Jung, W., Li, J., Chaudhuri, O. & Kim, T. Nonlinear elastic and inelastic properties of cells. *J. Biomech. Eng.* **142**, 1–18 (2020).

40. Andriotis, O. G., Desissaire, S. & Thurner, P. J. Collagen fibrils: Nature's highly tunable nonlinear springs. *ACS Nano.* **12**, 3671–3680 (2018).

41. Shima, S., Tatara, Y., Iio, M., Shu, C. & Lucero, C. J. Large deformations of a rubber sphere under diametral compression: part 2 : experiments on many rubber materials and comparisons of theories with experiments. *JSME Int. J. Ser. Mech. Mater. Eng.* **36**, 197–205 (1993).

42. Habbit, N. L. et al. Tunable three-dimensional engineered prostate cancer tissues for in vitro recapitulation of heterogeneous in vivo prostate tumor stiffness. *Acta Biomater.* **147**, 73–90 (2022).

43. Pradhan, S., Clary, J. M., Seliktar, D. & Lipke, E. A. A three-dimensional spheroidal cancer model based on PEG-fibrinogen hydrogel microspheres. *Biomaterials* **115**, 141–154 (2017).

44. Gonzalez-Fernandez, T., Tenorio, A. J., Saiz, A. M. & Leach, J. K. Engineered cell-Secreted extracellular matrix modulates cell spheroid mechanosensing and amplifies their response to inductive cues for the formation of mineralized tissues. *Adv. Healthc. Mater.* **11**, 1–13 (2022).

45. Parfenov, V. A. et al. Magnetic levitational bioassembly of 3D tissue construct in space. *Sci. Adv.* **6**, 1–12 (2020).

46. Guillaume, L. et al. Characterization of the physical properties of tumor-derived spheroids reveals critical insights for pre-clinical studies. *Sci. Rep.* **9**, 1–9 (2019).

47. James, J. D., Ludwick, J. M., Wheeler, M. L. & Oyen, M. L. Compressive failure of hydrogel spheres. *J. Mater. Res.* **35**, 1227–1235 (2020).

48. Glaubitz, M. et al. A novel contact model for AFM indentation experiments on soft spherical cell-like particles. *Soft Matter.* **10**, 6732–6741 (2014).

49. Ding, Y., Xu, G. K. & Wang, G. F. On the determination of elastic moduli of cells by AFM based indentation. *Sci. Rep.* **7**, 1–8 (2017).

50. Islam, M. T. et al. Non-invasive imaging of Young's modulus and Poisson's ratio in cancers in vivo. *Sci. Rep.* **10**, 1–12 (2020).

51. Bhagavathula, K. B., Meredith, C. S., Ouellet, S., Romanyk, D. L. & Hogan, J. D. Density, strain rate and strain effects on mechanical property evolution in polymeric foams. *Int. J. Impact Eng.* **161**, 104100 (2022).

52. Sun, Y. et al. The variation in elastic modulus throughout the compression of foam materials. *Acta Mater.* **110**, 161–174 (2016).

53. Ferraro, R., Caserta, S., Guido, S. A. & Low-Cost User-Friendly Rheo-Optical compression assay to measure mechanical properties of cell spheroids in standard cell culture plates. *Adv. Mater. Technol.* **9**, 1–11 (2024).

54. Hu, D. L., Phonekeo, S., Altshuler, E. & Brochard-Wyart, F. Entangled active matter: from cells to ants. *Eur. Phys. J. Spec. Top.* **225**, 629–649 (2016).

55. Rahimidehgolan, F. & Altenhof, W. Compressive behavior and deformation mechanisms of rigid polymeric foams: A review. *Compos. Part. B Eng.* **253**, 110513 (2023).

56. Peeters, E. A. G., Oomens, C. W. J., Bouten, C. V. C., Bader, D. L. & Baaijens, F. P. T. Viscoelastic properties of single attached cells under compression. *J. Biomech. Eng.* **127**, 237–243 (2005).

57. Ofek, G., Natoli, R. M. & Athanasiou, K. A. In situ mechanical properties of the chondrocyte cytoplasm and nucleus. *J. Biomech.* **42**, 873–877 (2009).

58. McGarry, J. P. Characterization of cell mechanical properties by computational modeling of parallel plate compression. *Ann. Biomed. Eng.* **37**, 2317–2325 (2009).

59. Guilak, F. Compression-induced changes in the shape and volume of the chondrocyte nucleus. *J. Biomech.* **28**, 1529–1541 (1995).

60. Trickey, W. R., Baaijens, F. P. T., Laursen, T. A., Alexopoulos, L. G. & Guilak, F. Determination of the Poisson's ratio of the cell: recovery properties of chondrocytes after release from complete micropipette aspiration. *J. Biomech.* **39**, 78–87 (2006).

61. Efremov, Y. M., Suter, D. M., Timashev, P. S. & Raman A. 3D Nanomechanical mapping of subcellular and sub-nuclear structures of living cells by multi-harmonic AFM with long-tip microcantilevers. *Sci. Rep.* **12**, 1–11 (2022).

62. Javanmardi, Y., Colin-York, H., Szita, N., Fritzsche, M. & Moeendarbary, E. Quantifying cell-generated forces: Poisson's ratio matters. *Commun. Phys.* **4**, 1–10 (2021).

63. Liu, K. K., Williams, D. R. & Briscoe, B. J. The large deformation of a single micro-elastomeric sphere. *J. Phys. D Appl. Phys.* **31**, 294–303 (1998).

64. Wenger, M. P. E., Bozec, L., Horton, M. A. & Mesquidaz, P. Mechanical properties of collagen fibrils. *Biophys. J.* **93**, 1255–1263 (2007).
65. Kain, L. et al. Calibration of colloidal probes with atomic force microscopy for micromechanical assessment. *J. Mech. Behav. Biomed. Mater.* **85**, 225–236 (2018).
66. Urcun, S. et al. Digital twinning of cellular capsule technology: emerging outcomes from the perspective of porous media mechanics. *PLoS One.* **16**, 1–30 (2021).
67. Pilato, C. A. et al. Isolation and characterization of cardiac mesenchymal stromal cells from endomyocardial bioptic samples of arrhythmogenic cardiomyopathy patients. *J. Vis. Exp.* 1–8 (2018). (2018).
68. Timoshenko, S. & Goodier, J. N. *Theory of Elasticity. Theory of elasticity* (McGraw-Hill, (1970).
69. Boussinesq, J. *Application Des Potentiels `aI´´etude De I´´equilibre Et Du Mouvement Des Solides ´elastiques* (Gauthier-Villars, 1885).
70. Hertz, H. Ueber die Berührung fester elastischer Körper. in *J Reine Angew Math* vol. 92 156–171De Gruyter, (1882).
71. Kar, S., Katti, D. R. & Katti, K. S. Evaluation of quasi-static and dynamic Nanomechanical properties of bone-metastatic breast cancer cells using a nanoclay cancer testbed. *Sci. Rep.* **11**, 1–16 (2021).
72. Hidaka, K. et al. Elasticity and viscoelasticity of embolization microspheres. *J. Mech. Behav. Biomed. Mater.* **4**, 2161–2167 (2011).
73. Dokukin, M. E., Guz, N. V. & Sokolov, I. Quantitative study of the elastic modulus of loosely attached cells in AFM indentation experiments. *Biophys. J.* **104**, 2123–2131 (2013).
74. Tatara, Y. Extensive theory of Force-Approach relations of elastic spheres in compression and in impact. *J. Eng. Mater. Technol.* **111**, 163–168 (1989).
75. Tatara, Y. On compression of rubber elastic sphere over a large range of displacements-part 1: theoretical study. *J. Eng. Mater. Technol. Trans. ASME.* **113**, 285–291 (1991).
76. Kim, K., Cheng, J., Liu, Q., Wu, X. Y. & Sun, Y. Investigation of mechanical properties of soft hydrogel microcapsules in relation to protein delivery using a MEMS force sensor. *J. Biomed. Mater. Res. Part. A.* **92A**, 103–113 (2010).
77. Wang, Z. & Liu, X. Adhesion of large-deformation elastic spherical contact. *Tribol Int.* **119**, 559–566 (2018).
78. Ding, Y., Wang, J., Xu, G. K. & Wang, G. F. Are elastic moduli of biological cells depth dependent or not? Another explanation using a contact mechanics model with surface tension. *Soft Matter.* **14**, 7534–7541 (2018).
79. Zhang, M. G., Cao, Y. P., Li, G. Y. & Feng, X. Q. Spherical indentation method for determining the constitutive parameters of hyperelastic soft materials. *Biomech. Model. Mechanobiol.* **13**, 1–11 (2014).
80. Ding, Y., Niu, X. R. & Wang, G. F. Compression of hyperelastic cells at finite deformation with surface energy. *Int. J. Appl. Mech.* **8**, 1–12 (2016).

Acknowledgements

Author contributions

D.G. acquired data from parallel-plate compression tests, performed formal data analysis, image analysis for tracking the lateral displacement, and contributed to the interpretation of the data. MP performed fixing, staining, and acquired 3D confocal fluorescence microscope images of CSs. R.C., E.C. provided the cardiac tissue biopsies and contributed to the development of CSs. M.S. extracted primary cardiac fibroblasts, prepared scaffold-free 3D cultures into CSs. M.D.B., contributed to the review and editing. A.R. contributed to the revision and editing of the work. G.J.S., P.J.T. and O.G.A., contributed to the conception of the study, the design of experiments, and the interpretation of the data, as well as to the revision and editing of the manuscript. All authors reviewed the manuscript.

Funding

Declarations

Competing interests

The authors declare no competing interests.

Additional information

Correspondence and requests for materials should be addressed to O.G.A.